

# Detailed Numerical Modeling and Simulation of $\text{Fe}_2\text{O}_3$ –Al Thermite Reaction

Kesiany M. de Souza<sup>[a]</sup> and Marcelo J. S. de Lemos<sup>\*[a]</sup>

**Abstract:** A thermite reaction is a self-propagating exothermic reaction with many practical applications in welding processes, material synthesis, pyrotechnic and initiator technologies. Motivated by the above-mentioned, the present study involves modeling and simulation of common hematite-aluminum thermite reaction with the aim of predicting temperature levels and radial burning speeds in a thin disk ignited at the center. Balance equations of species and energy conservation were solved in one dimension space by applying a finite difference method, considering no species transport and a one-step mechanism. The Arrhenius equation was adopted to model the kinetics rate. Phase change and temperature dependence of the thermochemical properties were also considered. Analyses of spatial and temporal meshes revealed that numerical results were independent of the grid used. Predictions show that

the ignition procedure affects the formation of the reaction-front, higher temperatures, and longer ignition zones can start the self-sustained reaction earlier. However, once the reaction wave is established, its velocity and peak temperature are the same, independent of the initial temperature profile. Simulations herein also show that an increase of the activation energy and decrease of the pre-exponential factor slows down the reaction speed considerably, impacting on accurate prediction of reaction-wave velocity. Further, the activation energy influences the burning velocity much more drastically than the pre-exponential factor. The maximum temperature observed in the model is around the melting temperature of alumina (2327 K), which is in agreement with the experimental results reported in the literature.

**Keywords:** Aluminothermic Reaction · Thermite · Finite-Difference-Scheme · Hematite-Aluminum Reaction

## 1 Introduction

A thermite reaction is a highly exothermic reduction-oxidation reaction with a production of great amounts of energy at high temperatures and a self-sustained behavior defined by the general reaction [1]



where a more active pure metal  $M$  reacts with a metal or non-metal oxide  $\text{AO}$ , resulting in a more stable oxide  $\text{MO}$ , metal or non-metal  $A$ , and energy  $Q$ . There are many possible compositions of thermite, most of them were summarized by Fischer and Grubelich [2]. Aluminum is the most commonly used fuel in the thermite-type reaction because of its high affinity for oxygen, easy handling, high boiling temperature, and abundance [3].

This reaction-type can react in oxygen-free environments due to the zero-oxygen balance of the reaction [4]. Also, they usually present condensed-phase products and the equation of state may no longer be valid, as commonly accepted in the  $\text{Fe}_2\text{O}_3$ –2Al thermite system, in which there is no pressure increase associated [5]. Gasless reactions are more stable since the kinetic rate is not affected by pressure variations, in other words, this kind of reaction is not significantly affected by external conditions. Therefore, the

reaction delay is the same whether the reaction takes place deep underwater or in a space vacuum [6].

The discovery of the displacement of oxygen contained in metal oxides by aluminum is credited to the Russian physicist Nikolay Beketov, who conducted experiments on aluminothermic reductions in 1865 at the University of Kharkiv in Ukraine [7]. Almost thirty years later, in 1893, the German Johannes Goldschmidt experimented with aluminothermic reactions to produce high purity chromium and manganese, which led him to patent the thermite process in 1895, and already in 1899, the thermite gained its first commercial application in rail welding in Essen [8]. Later, thermite gained other applications including a power plant patented by Johnson [9], the development of a high-regression solid fuel composition by Allen [10], and the aluminothermic production of metals and alloys [11]. Moreover, the use of thermite was adopted in the production of high-pressure gases at high velocities [12], high-temperature sintering and self-propagating (SHS) ceramics and composite materials [13], and the development of igniters [14]. Already

[a] K. M. de Souza, M. J. S. de Lemos  
Departamento de Energia – IEME  
Instituto Tecnológico de Aeronáutica – ITA  
12228-900 – São José dos Campos – SP, Brazil  
\*e-mail: delemos@ita.br

in the 21st century, we have studies of new applications of thermite in challenging environments such as welding in deep-water [15] and in space [16], well sealing and abandonment as patented by Skjold [17], and fabrication of lunar physical assets [18]. Recently, thermite reactions have been applied to develop a game change technology for plug and abandonment of depleted oil wells, which uses the released heat with the purpose of melting the production tubing and permanently close the borehole [19,20].

However, a detailed kinetic mechanism is still required for a deep investigation of all the factors affecting a thermite reaction. There is not even a consensus of measurement as it is difficult to measure experimentally the mechanism involved in such a fast and high-temperature reaction [21]. Also, experimental data of chemical kinetics and thermodynamics for metals or metal-containing compounds are scarce in literature [22], which makes it difficult to propose a detailed kinetic model for a thermite reaction, since experimental data is needed to build and validate a modeled chemical kinetic mechanism. Therefore, much experimental and theoretical research is still required to provide a more predictive model. As so, this lack of knowledge about all the physicochemical mechanisms involved in thermite reactions has led to simplified numerical studies [23].

Numerical simulations of reactions allow previewing peak temperatures, the energy released, propagation of the reaction, and other important aspects that are complex or expensive to analyze experimentally. However, most of the software available today is geared to working with gaseous reactions or reactions with a small amount of condensed phase. Most of them work with thermochemical equilibrium models, as CEA (Chemical Equilibrium with Analysis) from NASA [24,25], and they fail to converge for the reaction of compositions with a high concentration of solid species [6].

So, there are not many studies that numerically simulate the thermite reaction, and there is not yet a model that represents the development of a thermite reaction and that predicts and quantifies with precision all the parameters involved [21]. Zhu *et al.* [26] worked at a molecular level where they used the Molecular Dynamic method to model the reaction process and ignition performance. However, this method is limited to a relatively narrow frame of a few nanoseconds and it identifies processes that are, typically, considered as spontaneous in macroscopic simulations.

Baijot *et al.* [27] and Martirosyan *et al.* [28] have modeled mainly the pressure generation in thermite systems, which is more interesting for thermite systems composed of highly volatile species like  $\text{Al}/\text{Bi}_2\text{O}_3$  and  $\text{Al}/\text{CuO}$  systems. Brotman *et al.* [29] developed a condensed phase model to investigate the initial reaction stage in  $\text{Al}/\text{CuO}$  nano-system, however, they did not model the thermal losses as they were not interested in the whole macroscopic system but only in a two-nanoparticle pair system. Already Durães *et al.* [30] modeled the macroscopic  $\text{Fe}_2\text{O}_3$ –2Al thermite system and simulated the reaction front-propagation in a disk-shaped domain by solving the energy and species con-

servation equations, however, they assumed a constant kinetic rate, which disregards the temperature-sensitive kinetics of the reaction.

As so, this research aims to develop a model which predicts the temperature levels and the front-propagation behavior of the  $\text{Fe}_2\text{O}_3$ –2Al thermite reaction in a macroscopic system by applying the Arrhenius equation and a kinetics model suitable for condensed-phase reactions. Moreover, the temperature-dependence of the thermodynamic properties and also the phase changes involved in the reaction process were incorporated.

## 2 Mathematical Model

### 2.1 Problem Description

The problem analyzed is presented in Figure 1a, which was experimentally analyzed by Durães *et al.* [31], and numerically by Brito *et al.* [32] and Durães *et al.* [30]. The idea was to adopt these previous experimental and numerical studies as a foundation for our model. The domain consists of a thin thermite disk of a 25 mm radius, comprised between a stainless-steel recipient, and a PMMA (Poly-methyl methacrylate) disk. In the center of the thermite disk, there is an ignition zone with a 1.5 mm radius. The energy losses to the surroundings can be visualized in Figure 1b. Brito *et al.* [32] provided the values of the thermal transmittances. The thermite mixture is composed of aluminum (Al) and hematite ( $\text{Fe}_2\text{O}_3$ ).

### 2.2 Model Assumptions

For simplification purposes, it was considered a one-dimensional model in a disk-shaped domain. Also, the medium was considered static, without convection mechanisms. So, the following overall assumptions were made:

- One-dimensional radial non-steady propagation of the reaction;
- The initial mixture consists of reactants Al and  $\text{Fe}_2\text{O}_3$ , and Air, which is considered an inert gas that occupies voids in the formed porous medium;
- As aluminum melts at  $T_{\text{Al}}$ , the mixture compacts, and any porosity disappears;
- $\text{Fe}_2\text{O}_3$  is the reactant that controls the reaction;
- The mixture of reactants is considered to be homogeneous;
- The reaction is one-step, and all  $\text{Fe}_2\text{O}_3$  is consumed;
- No surface or particle dependent reactions;
- The movement of individual species or the mixture are not considered;
- The reaction rate depends on temperature and  $\text{Fe}_2\text{O}_3$  fraction;

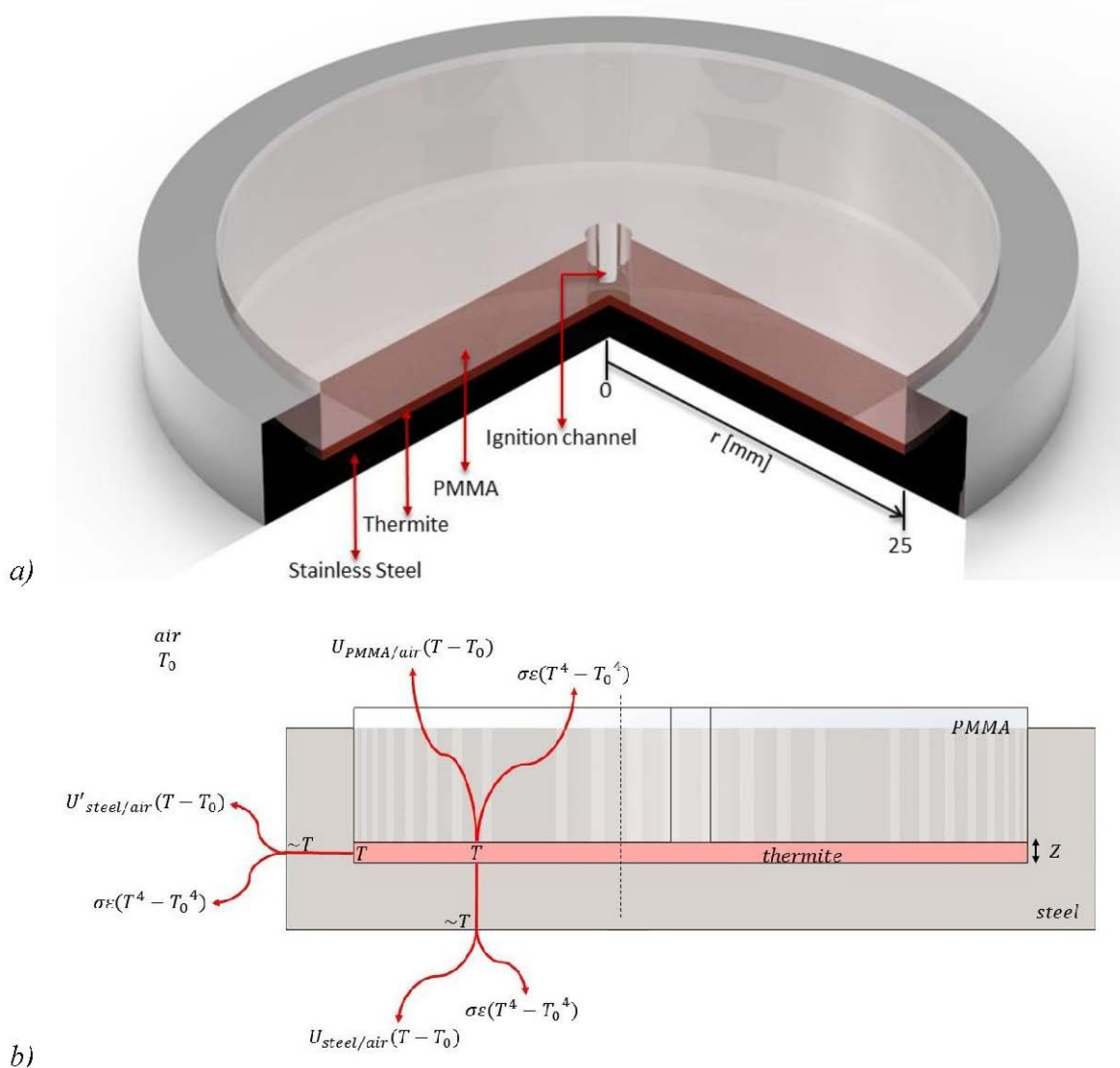


**Figure 1.** Computer-aided reproduction of the experimental setup from Durães et al. [31] and Durães et al. [30]: a) 3D design and components; b) thermal heat transfer through boundaries.

- The thermochemical properties vary with temperature whenever there is data available, and the species fractions.

### 2.3 Energy Equation

The transient behavior of temperature can be modeled by solving the equation of energy for one-dimensional heat transport in a radial domain as [33]

$$\rho c_p \frac{\partial T}{\partial t} = \frac{1}{r} \frac{\partial}{\partial r} \left( kr \frac{\partial T}{\partial r} \right) + S \quad (2)$$

where  $T$  is temperature,  $\rho$  is the density,  $c_p$  is the specific heat at constant pressure,  $k$  is the thermal conductivity,  $S$  is the source term which accounts for the energy released by the reaction and losses,  $r$  is the radius and  $t$  is time. Notice that the differential Eq. (2) has three terms, which are the accumulation or unsteady term, the diffusion term, and the source term. A convective term is not being considered since movement is not modeled in the present study.

### 2.4 Thermochemical Properties of the Mixture

The thermal capacity at constant pressure  $c_p$ , density  $\rho$ , thermal conductivity  $k$ , and emissivity  $\epsilon$  of the mixture were calculated using mixing rules as [30]

$$c_{PM} = \sum_i w_i c_{p,i} \quad (3)$$

$$\rho_M = \sum_i v_i \rho_i \quad (4)$$

$$\varepsilon_M = \sum_i v_i \varepsilon_i \quad (5)$$

$$k_M = \frac{\sum_i \frac{v_i}{k_i} + \sum_i v_i k_i}{2} \quad (6)$$

$$k_{Air,serial} = k_{Air} + 4\sigma\varepsilon_{Air}T^3v_{Air}\Delta r \quad (7)$$

where the subscript  $M$  accounts for a mixture property, the subscript  $i$  accounts for a species property,  $w$  and  $v$  are mass and volumetric fractions, respectively, and  $k_{Air,serial}$  is the equivalent conductivity of air in the serial arrangement accounting for the radiation on the void spaces.

The properties of each thermite species varying with temperature, whenever data was available, were retrieved from Brito *et al.* [32] and Chase *et al.* [34]. In the thermite mixture, the thermochemical properties were calculated accounting for porosity until aluminum fusion. This porosity was modeled through a volumetric fraction of Air  $v_{Air}=0.394$  as measured by Durães *et al.* [30]. However, as the air mass fraction is very small when compared to the other species involved in the mixture, its thermal capacity was not considered because it has an insignificant influence on the total thermal capacity of the mixture as calculated by Eq. (3).

## 2.5 Modeling Phase Changes

The phase changes of thermite species were modeled by the apparent heat capacity method of Bonacina and Comini [35], in which the enthalpy of fusion is modeled through modification of the specific heat capacity based on the temperature, resulting in the apparent heat capacity. The latent heat is added to the specific heat capacity of the melting material as it enters the fusion range. However, as the thermite species are pure materials, they melt at a specific fusion temperature  $T_F$ , and to apply this model for phase change, a temperature range must be defined. As so, it was considered a fusion range of  $T_F - \Delta T \leq T \leq T_F + \Delta T$ , with  $\Delta T = 5$  K. So, the apparent specific heat of a thermite species  $i$  could be modeled as

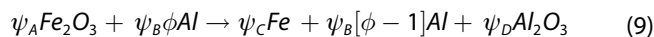
$$c_{p,i(apparent)} = \begin{cases} c_{p,i}(T) & T < T_F - \Delta T \text{ or } T > T_F + \Delta T \\ c_{p,i}(T) + \frac{L}{2\Delta T} & T_F - \Delta T \leq T \leq T_F + \Delta T \end{cases} \quad (8)$$

where  $c_{p,i(apparent)}$  is the apparent specific heat capacity of species  $i$ ,  $L$  is the enthalpy of fusion,  $2\Delta T$  is the temperature range in which the fusion takes place,  $c_{p,i}(T)$  is the specific heat capacity of species  $i$  at temperature  $T$ .

The enthalpy of fusion and fusion temperature for all thermite species considered were retrieved from thermochemical tables [34]. Notice that as hematite decomposes at 1473 K [36], its fusion is not treated. Already the aluminum oxide, since it has a decomposition temperature of 3250 K [27], which is higher than its fusion temperature of 2327 K [34], its fusion was modeled.

## 2.6 Chemical Reaction and Kinetics

The Fe<sub>2</sub>O<sub>3</sub>–2Al system reacts as



where  $\psi_i$  is the mass stoichiometric coefficient of the species  $i$  and  $\phi$  is the equivalence ratio. For a stoichiometric mixture,  $\phi = 1$ . Further, for ease of notation hereafter, in Eq. (9) the four chemical species involved can be identified by a subscript  $A$ ,  $B$ ,  $C$ , or  $D$ , as shown in Table 1. Due to the complexity of modeling the detailed kinetics of the reaction between aluminum and hematite, the present study was restricted to the reaction shown in Eq. (9), considering a one-step mechanism with only Fe, and Al<sub>2</sub>O<sub>3</sub> as products generated. Also, although reactants in Eq. (9) are combined as a permeable medium in which combustion takes place, in this work porosity is not considered when modeling the combustion process in porous media [37]. For a general formulation including porosity in the governing equations, the reader is referred to the work in [38]. Here, consistent with model assumptions above, as aluminum melts the mixture gets compacted and any porosity disappears.

As presented by Patankar [33], the conservation of a chemical species  $i$ , disregarding the convection and diffusion of the species, is expressed as

$$\frac{\partial}{\partial t}(\rho_m w_i) + \text{div}(\rho_m \mathbf{u} w_i + \mathbf{J}_i) = R_i \quad (10)$$

where  $\rho_m$  is the mixture density,  $w_i$  is the mass fraction of species  $i$ ,  $\mathbf{u}$  is the velocity field,  $\mathbf{J}_i$  the diffusion flux, and  $R_i$  is the rate of generation of the chemical species per unit vol-

**Table 1.** Mass stoichiometric coefficient of species involved in the model for the 2Al–Fe<sub>2</sub>O<sub>3</sub> reaction,  $\phi = 1$ .

Species	Species identifier	$\psi$
Fe <sub>2</sub> O <sub>3</sub>	$A$	–1.00000
Al	$B$	–0.33792
Fe	$C$	0.69943
Al <sub>2</sub> O <sub>3</sub>	$D$	0.63848

ume, caused by chemical reaction. Applying equation (10) to the species  $\text{Fe}_2\text{O}_3$ , the equation for conservation of this chemical species is

$$\frac{dW_A}{dt} = \psi_A r_k \quad (11)$$

where  $W_A = \rho_M w_A$  in  $[\text{kg}/\text{m}^3]$  is the mass concentration of hematite,  $\psi_A$  is the mass stoichiometric coefficient of hematite (see Table 1) and  $r_k$  is the kinetic rate of reaction, which will be discussed later.

As the stoichiometric mixture was investigated, the initial mass fractions of the reagents were set as presented in Table 2.

The values assumed for the mass stoichiometric coefficients  $\psi$  of each species are shown in Table 1, where for each 1 kg of hematite and 0.33792 kg of aluminum consumed, 0.69943 kg of iron and 0.63848 kg of alumina is produced. Here, the governing equation for all species is based on hematite concentration variation, Eq. (11), since the concentration of other species can be determined as

$$W_B = W_{B0} - \frac{\psi_B}{\psi_A} \eta W_{A0} \quad (12)$$

$$W_C = W_{C0} - \frac{\psi_C}{\psi_A} \eta W_{A0} \quad (13)$$

$$W_D = W_{D0} - \frac{\psi_D}{\psi_A} \eta W_{A0} \quad (14)$$

where  $W_{A0}$ ,  $W_{B0}$ ,  $W_{C0}$ , and  $W_{D0}$  are the initial mass concentration of hematite, aluminum, iron, and alumina, respectively, and  $\eta$  is the extent of the reaction determined as

$$\eta = \frac{W_{A0} - W_A}{W_{A0}} \quad (15)$$

The extent of the reaction  $\eta$  is 0 before the reaction starts and 1 when the reaction is complete and all  $\text{Fe}_2\text{O}_3$  is consumed. It is not equivalent to time and, as so, it does not represent the time-evolution of the reaction as explained by Baijot [21].

In order to determine the kinetic rate  $r_k$ , we must relate it to the extension of the reaction to be able to apply Eq. (2) presented in Section 2.3. To do so, we can derivate equation (15) as

$$\frac{d\eta}{dt} = -\frac{1}{W_{A0}} \frac{dW_A}{dt} \quad (16)$$

Substituting Eq. (11) into (16) we have

$$\frac{d\eta}{dt} = -\frac{\psi_A}{W_{A0}} r_k \quad (17)$$

As the multiple steps and diffusion effects involved in condensed-phase reactions are complex to model, simplification is necessary to make possible a mathematical analysis. As so, a single-step kinetics approximation can be applied in which the reaction rate depends on temperature and the extent of the reaction as [6, 39]

$$\frac{d\eta}{dt} = A_F e^{-E_A/RT} (1 - \eta)^N \quad (18)$$

Finally, substituting Eq. (18) for a 1<sup>st</sup>-order kinetics ( $N=1$ ) into Eq. (17), and reorganizing the terms, we can determine the rate at which the hematite is consumed as

$$r_k = -\frac{W_{A0}}{\psi_A} A_F e^{-E_A/RT} (1 - \eta) \quad (19)$$

As cited before, the present reaction model investigates the reaction propagation experimentally analyzed by Durães *et al.* [31], but they measured only the burning speed of the  $\text{Fe}_2\text{O}_3$ -2Al system and no data of the kinetics parameters are given. So, the Arrhenius parameters were initially calibrated to match the measured burning velocity at stoichiometric conditions. To do so, it was assumed the activation energy of 158 kJ/mol was measured by Sahoo *et al.* [40] for the stoichiometric  $\text{Fe}_2\text{O}_3$ -2Al system. Then, the pre-exponential factor was calibrated in order to the numerical burning velocity match the experimental result from Durães *et al.* [31]. Moreover, the effects of varying the Arrhenius kinetic parameters were investigated in the present study.

## 2.7 Source Term for the Energy Equation

For the disk-shaped problem, the source term  $S$  in Eqn. (2) considers both the energy generated by the reaction and the energy loss to the environment by radiation and conduction mechanisms through the PMMA plate at the top of the control-volume and through the stainless-steel plate at the bottom surface of the control volume, as shown in Figure 1b. It is, accordingly, defined as

$$S_{\text{disk}} = Qr_k - [(U_{\text{steel/air}} + U_{\text{PMMA/air}})(T - T_0) + 2\sigma\epsilon(T^4 - T_0^4)]/Z \quad (20)$$

**Table 2.** Initial mass fractions.

$\phi$	$W_{A0}$	$W_{B0}$
1,00	0.7474	0.2526

where  $Q$  is the combustion energy released to the surroundings by 1 kg of hematite consumed in [J/kg], and  $r_k$  is the volumetric rate at which the hematite is consumed, given in [kg/m<sup>3</sup>s]. Therefore, the energy generation term  $Qr_k$  is given in [J/m<sup>3</sup>s]. The second term on the right-hand side of Eq. (20) is an absorber, where energy is lost by conduction and radiation,  $\sigma$  is the Boltzmann constant,  $\epsilon$  is the thermite mixture emissivity,  $T$  is the thermite temperature,  $T_0$  is the external environment temperature,  $Z$  is the thermite plate thickness and  $U_{\text{steel/air}}$  and  $U_{\text{PMMA/air}}$  are the thermal transmittance at the top and bottom faces of the domain. The last three parameters were provided by Brito *et al.* [32] as 1.5 mm, 4.96 W/(m<sup>2</sup>K), and 3.91 W/(m<sup>2</sup>K), respectively.

The energy released by the reaction to the surroundings can be determined as a function of temperature as [41]

$$Q = H_{\text{reac}}(T_{\text{ref}}) - \Delta h_{s,p}(T_p) \quad (21)$$

where  $H_{\text{reac}}$  is the enthalpy of combustion at standard conditions in [J/kg] of hematite consumed, calculated from thermochemical tables [34], as

$$H_{\text{reac}} = 5323911.03 \text{ J/kg} \quad (22)$$

and  $\Delta h_{s,p}(T_p)$  is the sensible enthalpy variation of the products from the reference temperature to the temperature of the product. The sensible enthalpy of the products was determined from the sensible enthalpy of each species taken from thermochemical tables [34], considering the phase transitions.

As so, the calculated energy released in the function of temperature is shown in Figure 2. Observe that the adiabatic flame temperature for this thermite reaction is about

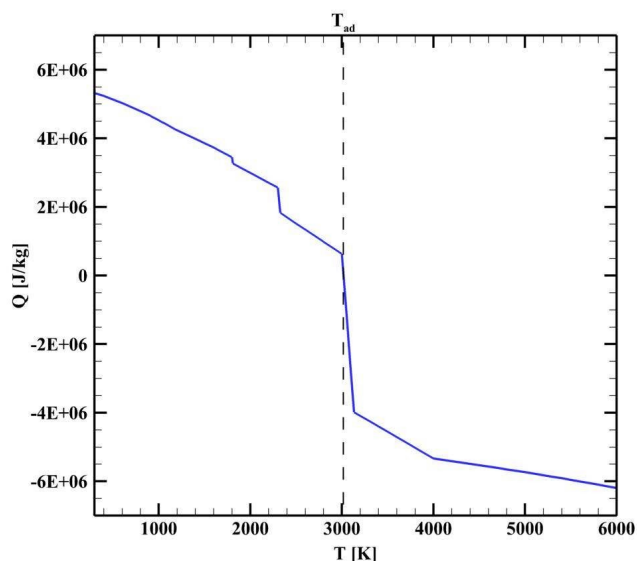


**Figure 2.** Energy released by the reaction  $2\text{Al-Fe}_2\text{O}_3$  at constant pressure, as a function of the temperature of reaction.

3000 K where the enthalpy of products matches the enthalpy of reagents, resulting in zero energy release. The figure indicates that at a temperature higher than the adiabatic one, this reaction becomes endothermic, in other words, energy needs to be added in order for the products to reach these high temperatures.

## 2.8 Initial and Boundary Conditions

A temperature of 298 K was applied as an initial condition in all domains, except at  $0 \leq r \leq 1.5$  mm (see Figure 1), where an ignition temperature of 1500 K was defined.

### Inner Boundary ( $r = 0$ mm):

At the inner boundary, a symmetric condition was applied since there can be no heat flux at this boundary because of the symmetric geometry:

$$\left(\frac{\partial T}{\partial r}\right)_{r=0} = 0 \quad (23)$$

### Outer Boundary ( $r = 25$ mm):

At the outer boundary, a conductive/radiative flux is given as proposed by Brito *et al.* [32]

$$k\left(\frac{\partial T}{\partial r}\right)_{r=R} = -\left[U'_{\text{steel/air}}(T - T_0) + \sigma\epsilon(T^4 - T_0^4)\right] \quad (24)$$

where they determined the thermal transmittance  $U'_{\text{steel/air}}$  as 5.94 W/(m<sup>2</sup>K). The representation of this boundary condition can be seen in Figure 1b.

## 3 Numerical Model

To numerically solve the governing Eqns. (2) and (11), firstly, the domain was discretized in  $im$  points equally distributed along  $r$ -direction, with a distance between any neighbor points of  $\Delta r$ . Then, the equations were modeled by applying a finite-difference method (FDM), which solves differential equations by approaching the derivatives as finite differences. Following this methodology, the conservation equations were discretized and applied to the geometries investigated, as detailed in the following subsections. In this work, a semi-implicit formulation in time was employed as it will be shown next.

### 3.1 Energy Equation

The finite difference methodology was applied to model the partial derivatives in time and space presented in the energy conservation Eq. (2). Firstly, this equation was expanded as:



$$\rho c_p \frac{\partial T}{\partial t} = \frac{k}{r} \frac{\partial T}{\partial r} + \frac{\partial}{\partial r} \left( k \frac{\partial T}{\partial r} \right) + S \quad (25)$$

where the second-order partial derivative in  $r$  was expanded by applying the chain-rule formulation. Then, the partial derivative in time was modeled by a forward-first-order finite difference scheme. Already the partial derivatives in  $r$  were discretized by a fourth-order central difference scheme. As all partial derivatives of the energy conservation equation could be numerically modeled by a finite difference scheme, this equation can now be presented as an algebraic equation:

$$a_i T_i^n = b_i T_{i+1}^n + c_i T_{i-1}^n + e_i T_{i+2}^n + f_i T_{i-2}^n + d_i \quad (26)$$

where the coefficients are determined as:

$$a_i = \left( 1 + \frac{\alpha_{ce} \Delta t}{\Delta r^2} \right) \quad (27)$$

$$b_i = \left( \frac{\alpha_{fo+1} \Delta t}{\Delta r^2} + \frac{2\alpha \Delta t}{3r_i \Delta r} \right) \quad (28)$$

$$c_i = \left( \frac{\alpha_{ba-1} \Delta t}{\Delta r^2} - \frac{2\alpha \Delta t}{3r_i \Delta r} \right) \quad (29)$$

$$e_i = \left( -\frac{\alpha_{fo+2} \Delta t}{\Delta r^2} - \frac{\alpha \Delta t}{12r_i \Delta r} \right) \quad (30)$$

$$f_i = \left( -\frac{\alpha_{ba-2} \Delta t}{\Delta r^2} + \frac{\alpha \Delta t}{12r_i \Delta r} \right) \quad (31)$$

$$d_i = \frac{S_i^{n-1} \Delta t}{\rho_i^{n-1} c_p i^{n-1}} + T_i^{n-1} \quad (32)$$

In the above equations, the terms  $\alpha$  contain the thermal conductivity discretization as shown in the equation below:

$$\alpha = \frac{k_i^{n-1}}{\rho_i^{n-1} c_p i^{n-1}} \quad (33)$$

$$\alpha_{ce} = \frac{1}{8} \left( \frac{k_{i+2}^{n-1} + 16k_{i+1}^{n-1} + 18k_i^{n-1} + 16k_{i-1}^{n-1} + k_{i-2}^{n-1} + k_{i-2}^{n-1}}{\rho_i^{n-1} c_p i^{n-1}} \right) \quad (34)$$

$$\alpha_{fo+1} = \frac{1}{2} \left( \frac{k_{i+2}^{n-1} + 3k_{i+1}^{n-1} + 3k_i^{n-1} + k_{i-1}^{n-1}}{\rho_i^{n-1} c_p i^{n-1}} \right) \quad (35)$$

$$\alpha_{ba-1} = \frac{1}{2} \left( \frac{k_{i+1}^{n-1} + 3k_i^{n-1} + 3k_{i-1}^{n-1} + k_{i-2}^{n-1}}{\rho_i^{n-1} c_p i^{n-1}} \right) \quad (36)$$

$$\alpha_{fo+2} = \frac{3}{8} \left( \frac{k_i^{n-1} + k_{i+2}^{n-1}}{\rho_i^{n-1} c_p i^{n-1}} \right) \quad (37)$$

$$\alpha_{ba-2} = \frac{3}{8} \left( \frac{k_i^{n-1} + k_{i-2}^{n-1}}{\rho_i^{n-1} c_p i^{n-1}} \right) \quad (38)$$

At  $i=2$ , and  $i=im$  a three-point central-difference scheme was applied as:

$$a_i T_i^n = b_i T_{i+1}^n + c_i T_{i-1}^n + d_i \quad (39)$$

where the coefficients  $e_i$  and  $f_i$  are null.

By applying the same methodology used to derive the coefficients of the five-point equation, we have the definition of the coefficients of Eq. (39) as:

$$a_i = 1 + \frac{2\alpha_{ce} \Delta t}{\Delta r^2} \quad (40)$$

$$b_i = \frac{\alpha_{fo} \Delta t}{\Delta r^2} + \frac{\alpha \Delta t}{2r_i \Delta r} \quad (41)$$

$$c_i = \frac{\alpha_{ba} \Delta t}{\Delta r^2} - \frac{\alpha \Delta t}{2r_i \Delta r} \quad (42)$$

$$d_i = \frac{S_i^{n-1} \Delta t}{\rho_i^{n-1} c_p i^{n-1}} + T_i^{n-1} \quad (43)$$

where:

$$\alpha = \frac{k_i^{n-1}}{\rho_i^{n-1} c_p i^{n-1}} \quad (44)$$

$$\alpha_{ba} = \frac{k_i^{n-1} + k_{i-1}^{n-1}}{2\rho_i^{n-1} c_p i^{n-1}} \quad (45)$$

$$\alpha_{fo} = \frac{k_{i+1}^{n-1} + k_i^{n-1}}{2\rho_i^{n-1} c_p i^{n-1}} \quad (46)$$

$$\alpha_{ce} = \frac{k_{i+1}^{n-1} + 2k_i^{n-1} + k_{i-1}^{n-1}}{4\rho_i^{n-1} c_p i^{n-1}} \quad (47)$$

Notice the temperature is effectively determined at the time step  $n$ , while the thermal properties are evaluated at the time step  $n-1$ . As so, the method applied is not completely implicit since data from the previous time step is being carried out to the present time step.

By applying Eq. (26) to all points inside the domain, there will be a system composed of a square penta-diagonal matrix of dimension  $im$ :

$$\begin{bmatrix} -a_1 & b_1 & e_1 & 0 & \cdots & \cdots & 0 \\ c_2 & -a_2 & b_2 & e_2 & \ddots & & \vdots \\ f_3 & c_3 & \ddots & \ddots & \ddots & \ddots & \vdots \\ 0 & f_4 & \ddots & \ddots & \ddots & e_{im-3} & 0 \\ \vdots & \ddots & \ddots & \ddots & \ddots & b_{im-2} & e_{im-2} \\ \vdots & & \ddots & f_{im-1} & c_{im-1} & -a_{im-1} & b_{im-1} \\ 0 & \cdots & \cdots & 0 & f_{im} & c_{im} & -a_{im} \end{bmatrix} \quad (48)$$

$$\begin{bmatrix} T_1 \\ T_2 \\ T_3 \\ \vdots \\ T_{im-2} \\ T_{im-1} \\ T_{im} \end{bmatrix} = \begin{bmatrix} -d_1 \\ -d_2 \\ -d_3 \\ \vdots \\ -d_{im-2} \\ -d_{im-1} \\ -d_{im} \end{bmatrix}$$

where the coefficients  $f_1, f_2, c_1, b_{im}, e_{im},$  and  $e_{im-1}$  are zero since they accompany points outside the domain.

To solve this system with minimum computational work, it was applied the tri-diagonal algebraic solution, known as Thomas Algorithm, adapted for a penta-diagonal array as proposed by Fletcher [42] and Nieckele [43].

### 3.2 Boundary Conditions

#### Inner Boundary ( $r=0$ mm):

As  $T_1 = T_2$ , the coefficients of the linear algebraic Eq. (26) are defined as:

$$a_1 = 1; \quad b_1 = 1; \quad d_1 = 0; \quad e_1 = 0$$

#### Outer Boundary ( $r=25$ mm):

Approaching the partial derivative term of Eq. (24) by a first-order backwards scheme:

$$k_{im}^{n-1} \left( \frac{T_{im}^n - T_{im-1}^n}{\Delta r} \right) = - \left[ U_{steel/air}^{n-1} (T_{im}^{n-1} - T_0) + \sigma \varepsilon ((T_{im}^{n-1})^4 - T_0^4) \right] \quad (49)$$

As so, by isolating the term  $T_{im}^n$  we have:

$$T_{im}^n = T_{im-1}^n - \frac{\Delta r}{k_{im}^{n-1}} \left[ U_{steel/air}^{n-1} (T_{im}^{n-1} - T_0) + \sigma \varepsilon ((T_{im}^{n-1})^4 - T_0^4) \right] \quad (50)$$

Therefore, the coefficients of Eq. (26) applied to this boundary are:

$$a_{im} = 1; \quad c_{im} = 1; \quad d_{im} = - \frac{\Delta r}{k_{im}^{n-1}} \left[ U_{steel/air}^{n-1} (T_{im}^{n-1} - T_0) + \sigma \varepsilon ((T_{im}^{n-1})^4 - T_0^4) \right]; \quad f_{im} = 0;$$

### 3.3 Species Conservation Equation

To model the first-order time derivative in Eq. (11), a backward first-order difference scheme in  $t$  was applied as:

$$\frac{dW_A}{dt} \approx \frac{W_{A,i}^n - W_{A,i}^{n-1}}{\Delta t} \quad (51)$$

Substituting Eq. (51) into Eq. (11) and reorganizing terms the mass concentration of Fe<sub>2</sub>O<sub>3</sub> at time  $t + \Delta t$  can be determined as:

$$W_{A,i}^n = \psi_A r_{tc} \Delta t + W_{A,i}^{n-1} \quad (52)$$

### 3.4 Implementation of the Numerical Model

To solve the discretized equations of mass transport and energy conservation through the domain analyzed, an algorithm was developed as shown in Figure 3 and implemented in a C programming language, and compiled in Dev C++ [44]. Firstly, the thermochemical data and all parameters required are imported. Next, the grid and variables are initialized, followed by a temporal loop. Inside this loop, the equations are solved at each node and each time step. The solution starts with the calculation of the reaction rate by Eq. (19) with temperature from previous time step  $T(t-dt)$ , then, the species fractions at all nodes are determined by Eqns. (52), (12), (13), and (14). Observing that when the aluminum fuses, the porosity is no longer considered and the volume fraction of air is then set to zero, and the fractions of the remaining species are recalculated.

With the species fraction determined, the thermodynamic properties can then be retrieved from the imported data at each node for each thermite species or material, considering the temperature of the previous time step  $T(t-dt)$ . Then, the apparent specific heat of each species or material is calculated from Eq. (8), which adds the enthalpy of fusion to the specific heat of the species if the temperature is inside the range of phase change. Then the mixing rules



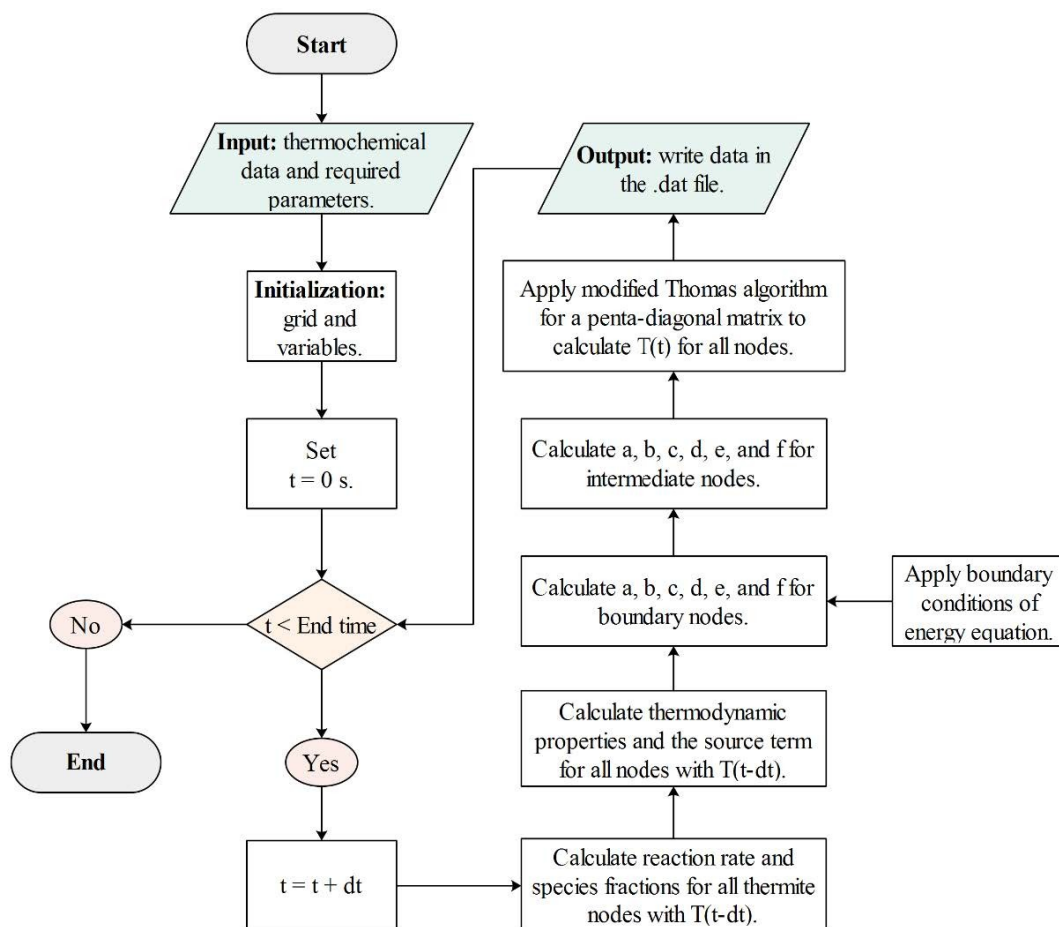


Figure 3. Flow-chart of the algorithm applied to solve the species and energy conservation equations.

can be applied as presented in Eqs. (3), (4), (5), (6), and (7) at the thermite nodes.

Next, the source term is calculated from Eq. (20) with temperature from previous step  $T(t-dt)$  and the already previously calculated reaction rate. As the thermochemical properties and source term at each node have been calculated, the coefficients of the penta-diagonal matrix can be determined, considering the boundary conditions. Finally, the modified Thomas algorithm is applied to solve for temperature  $T(t)$  at all nodes. Then, the data at time  $t$  is saved in a .dat file, which closes the loop. The loop stops when an End time is reached.

Notice that the numerical model applied is not fully-implicit because, although the temperature profile is calculated at time  $t$  by solving a system of linear equations in which the temperature at each node are the unknowns, the thermodynamic properties, reaction rate, and source term are determined with temperature profiles from time  $t-dt$ .

## 4 Results and Discussion

### 4.1 Validation of the Model

In this section, a convergence study is carried out to determine the optimum radial and time steps. As the front-propagation of the thermite reaction modeled is fast (27 mm/s), the mesh and time step must be small enough to capture the results with a good approach. Also, if the time step adopted is very coarse, it will not be able to capture phase changes since the apparent  $C_p$  method was applied as explained in Section 2.5.

#### 4.1.1 Mesh Convergence

In order to perform the mesh convergence analysis, the reaction duration,  $t_r$ , or time it takes for the reagents to be completely consumed at the mid-radius ( $r = 0.0125$  m) was calculated for four meshes with nodes equally spaced, as represented by the delta symbols shown in Figure 4. The re-

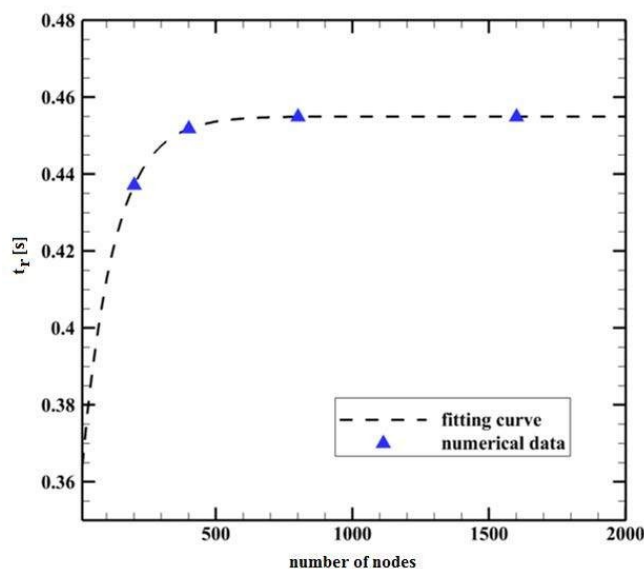


**Figure 4.** Mesh convergence analysis: reaction time at mid radius ( $r=0.0125$  m) in function of the number of nodes.

action duration was determined as the time it takes for  $\eta$  to vary from 0.001 to 0.999. The meshes simulated have 201, 401, 801, and 1601 nodes. Observing the fitting curve shown in Figure 4, the mesh with 801 nodes is already converged as will be discussed in more detail next.

To better observe the mesh convergence, Figure 5 shows the temperature profiles for the four meshes analyzed in different moments. The meshes with 801 and 1601 nodes resulted in overlapped profiles, while the mesh with 401 resulted in a slightly faster front propagation, followed by the mesh with 201 nodes. Observing that, the mesh with 801 nodes was selected since it shows to be the best choice.

Notice that, as the mesh is more refined, it takes a longer time to complete the reaction as could be observed in Figure 4, which slows down the reaction propagation in agreement with results shown in Figure 5.

#### 4.1.2 Time Step Analysis

The effect of decreasing the time step was evaluated as shown in Figure 6a and Figure 6b, where four time-steps were analyzed. Notice that the highest time-step ( $\Delta t=1 \times 10^{-3}$ ) underestimates the velocity of the front-propagation, while the others do not show notable differences observable in these figures.

However, another important parameter must be observed to choose an optimum time step: the specific heat capacity. As explained before, the phase change of a determined species is modeled by adding the required enthalpy of fusion to its specific heat capacity as the temper-

ature reaches the phase change range, as explained in Section 2.5, which results in a peak in the profile of specific heat of the mixture, as shown in Figure 7. The three peaks observed are from the aluminum, iron, and alumina fusion, respectively. The highest time step did not capture any of these peaks, which explains the higher temperatures observed in Figure 6.

Also, observing Figure 7, the time step of  $1 \times 10^{-4}$  s resulted in a slightly faster propagation wave, which is notable as the phase-change peaks appeared at the mid-radius ( $r=0.0125$  m) first for the simulation with this time step, while the others smaller time steps show overlapped profiles. Therefore, the time step of  $1 \times 10^{-5}$  s was selected as the optimum value not only to capture the phase changes but also to capture the front-velocity propagation with more precision.

#### 4.2 Characterization of the Reaction Wave Propagation

Figure 8 illustrates the reaction wave propagation observed for the calibrated model ( $E_A=158$  kJ/mol;  $A_F=2.2 \times 10^6$  s $^{-1}$ ). It follows the typical self-propagating reaction wave composed of two zones described by Kim [45]. In the reaction zone, the extension of the reaction ( $\eta$ ) rapidly varies from one to zero while the reaction takes place represented by the reaction rate ( $r_k$ ). The temperature does not change so rapidly, in fact, it has a slow variation at the preheating zone as the heat diffuses ahead of the wave and increases the temperature from the ambient temperature to the ignition temperature, and a more sharply variation at the reaction zone as energy is released by the consumption of the reactants, increasing the temperature from the ignition temperature to the peak temperature.

The reaction wave propagation across the entire domain can be observed in Figure 9, where the temperature profiles at different times are plotted. Notice that after the ignition zone ( $0 \leq r \leq 0.0015$  m), the reaction propagates at a nearly constant velocity until it approaches the outer boundary ( $r=0.025$  m). Also, the peak temperature ( $T_p$ ) does not have a significant variation inside the domain, away from the boundaries.

The peak temperature reached behind the wave is 2325 K, which is nearly the fusion temperature of alumina of 2327 K [34]. What happens is that the temperature reaches the range of alumina fusion considered in the model ( $2322 \text{ K} < T < 2332 \text{ K}$ ), but the energy generated is not enough to overcome the energy losses and also completely melt the alumina presented in the products, which works as a barrier to achieve higher temperature levels. As so, higher temperatures are only noticed at the ignition zone ( $0 \leq r \leq 0.0015$  m), caused by the ignition energy initially provided to start the self-sustained reaction of thermite, and also near the outer boundary ( $r=0.025$  m), caused by a small energy accumulation due to the slower heat transfer through the outer boundary in comparison to the fast en-

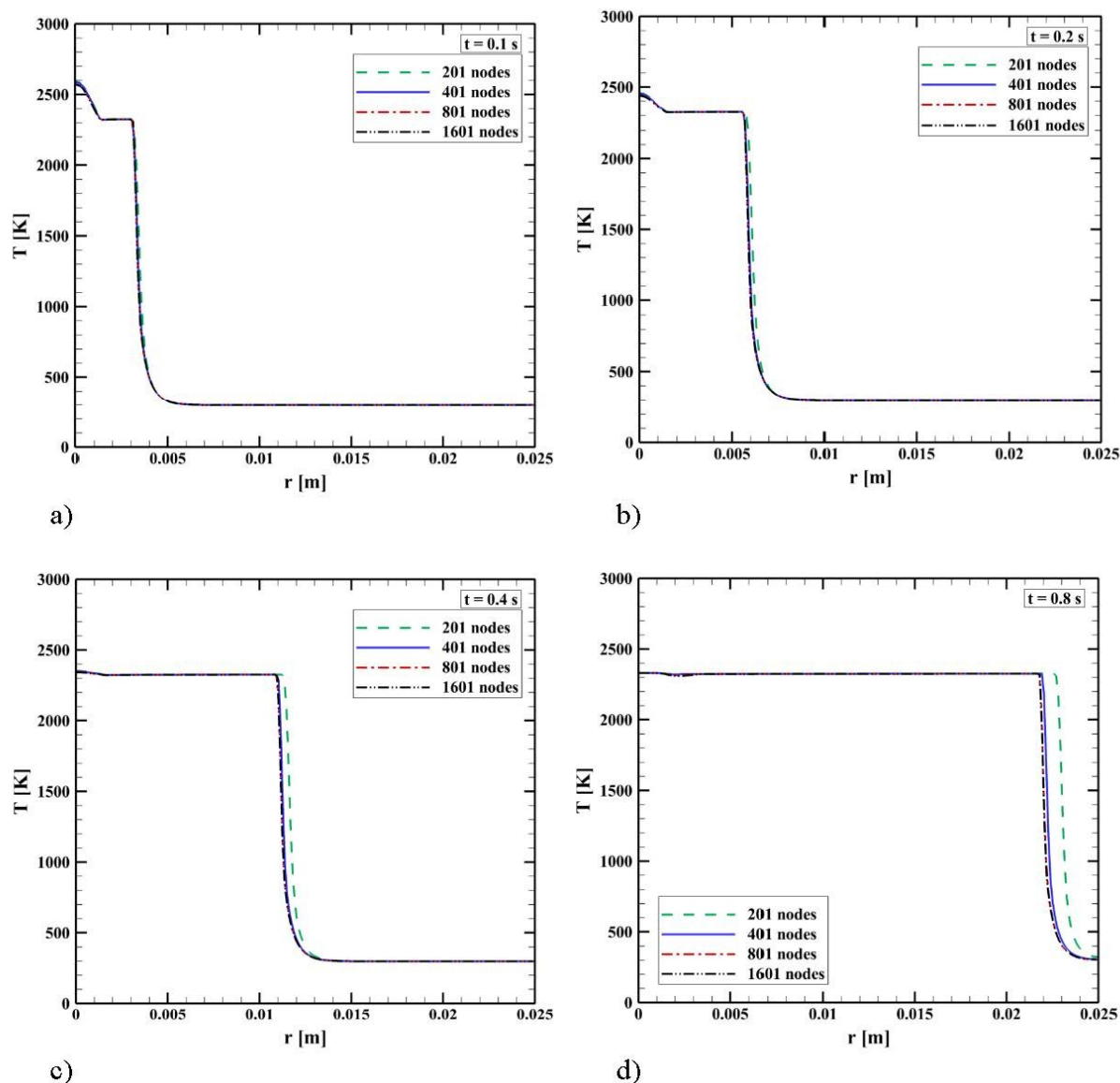


Figure 5. Mesh convergence analysis: temperature profiles at a) 0.1 s; b) 0.2 s; c) 0.4 s; d) 0.8 s.

ergy generated at this zone. These zones of higher temperatures were also observed by Durães *et al.* [30].

The temperature contours and profiles are also presented in Figure 10, where it gives us a better notion of how the reaction wave propagates and also the temperature decay after the wave has swept all the domain. The reaction wave is a narrow region with high-temperature gradients and it takes less than 1 s to sweep the entire domain, as also observed in Figure 9. Then, the temperature of the domain decays slowly and quite evenly, which takes approximately 50 s to decrease the temperature to 1000 K.

#### 4.2.1 Effect of the Ignition Procedure

According to Zhang and Stangle [46], a self-propagating combustion process is considered ignited if the reaction is initiated and then, it is self-propagating. For that, the local rate of energy generation must be large enough to overcome the energy redistribution caused by conduction, convection, and radiation. As so, low thermal conductance, low heat capacity, small particle sizes, and high energy of reaction are important to promote ignition [6]. As cited by Meir and Jerby [47], thermite is much harder to ignite than common explosives. This is associated with the high thermal conductivity of the metal and the metal oxide, which requires a large amount of preheating energy to compen-

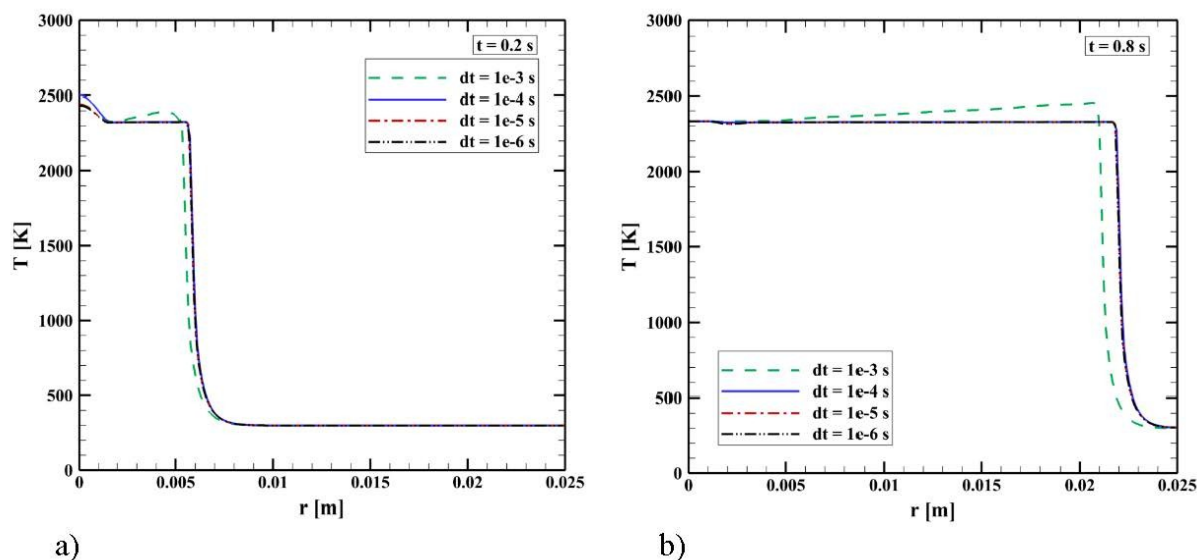


**Figure 6.** Time step analysis: temperature profiles at a) 0.2 s; b) 0.8 s.

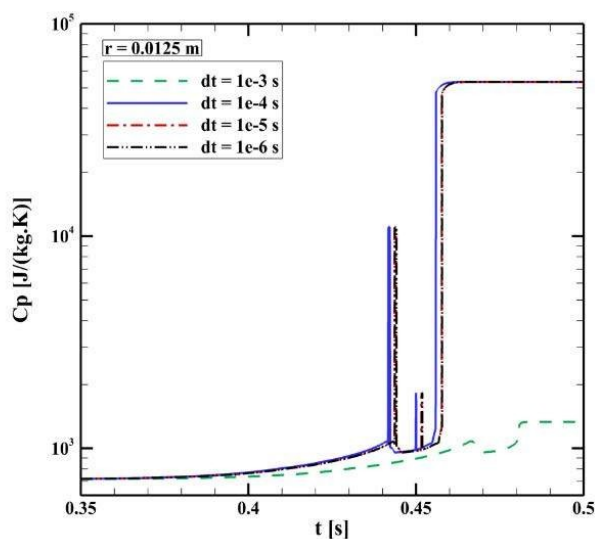


**Figure 7.** Time step analysis: effect of the time step on the specific heat capacity of the mixture.

sate for the energy loss to the surrounding environment, as also explained by Sui [48].

As so, the ignition of the thermite reaction was investigated in the present study. As explained in Section 2.8, the ignition procedure of the thermite was modeled by setting an initial temperature at the ignition zone ( $0 \leq r \leq 0.0015$  m) of 1500 K. This assumption was enough to start the self-propagated reaction. However, different profiles of temperature could be initially assumed, as represented in Figure 11a.

It was noticed that the minimum temperature that must be set in the assumed ignition zone ( $0 \leq r \leq 0.0015$  m) is 1306 K, to trigger the reaction. Lower temperatures were not enough, as can be observed for the profile with 1250 K at this ignition zone. However, when a longer ignition zone of ( $0 \leq r \leq 0.0050$  m) was set with an initial temperature of 1250 K, this input energy was enough to start the self-sustained reaction. As so, the reaction wave can be started with lower temperatures if the ignition zone is long enough. Cheng *et al.* [49] and Sarangi *et al.* [50] measured the ignition temperature of the  $\text{Fe}_2\text{O}_3$ –2Al thermite reaction as 1299.2 K, and 1200 K, respectively, which are close to the values observed in the present study.

Also, observing Figure 12, the final velocity reached by all reaction waves formed is the same, independently of the initial temperature profile. The ignition procedure only affects the initial formation of the reaction-front. Higher temperatures and longer ignition zones can start the self-sustained reaction faster. However, once the reaction wave is established, its velocity and peak temperature are the same independent of the initial temperature profile.

### 4.3 Investigation of the Kinetics Parameters

The results observed previously had the assumption of an n-order kinetics model as presented by Eq. (18), with the activation energy assumed as the same experimentally measured by Sahoo *et al.* [40] for the stoichiometric mixture of  $\text{Fe}_2\text{O}_3$ –2Al. As explained in section 2.6, the pre-exponential factor was then calibrated to result in the same front-propagation velocity observed experimentally by Durães *et al.* [31]. However, the effect of activation energy and pre-ex-

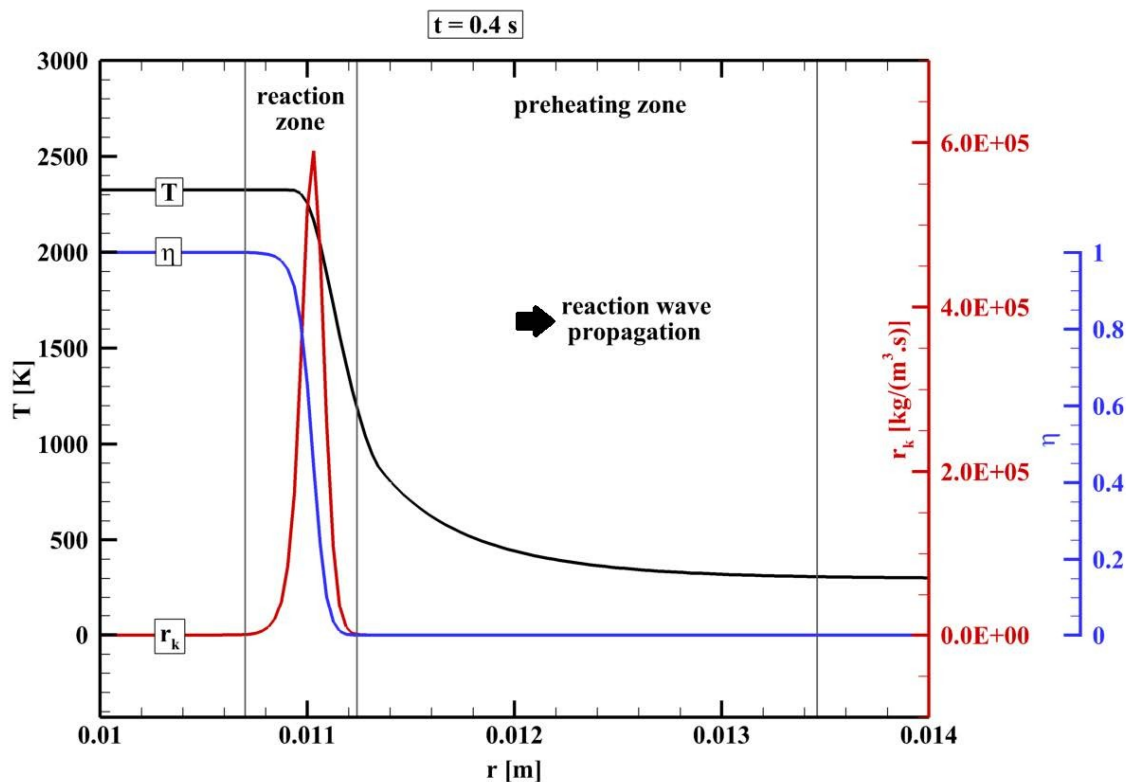


**Figure 8.** Reaction zone and preheating zone observed at  $t = 0.4$  s for the calibrated case with the Arrhenius parameters  $E_A = 158$  kJ/mol and  $A_f = 2.2 \times 10^6$  s $^{-1}$ .

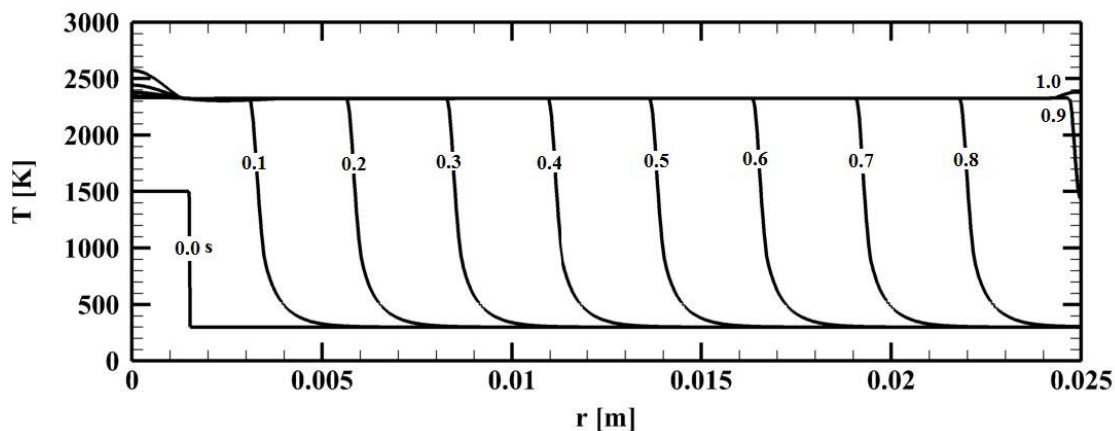


**Figure 9.** Reaction wave propagation along the radial direction.

ponential factor on the velocity and peak temperature of the reaction wave must be evaluated. It is important to understand the limits of assuming specific kinetic parameters, and the importance of experimental data to model a reaction wave with accuracy.

As so, various simulations were carried out varying only the activation energy and keeping the pre-exponential fac-

tor as  $2.2 \times 10^6$  s $^{-1}$ , and others varying only the pre-exponential factor and keeping the activation energy as 158 kJ/mol. The results for the velocity of the reaction wave are shown in Figure 13. It is perceptible the opposite effects of these kinetic parameters. While an increase in activation energy slows down the front propagation, an increase in the pre-exponential factor accelerates it.



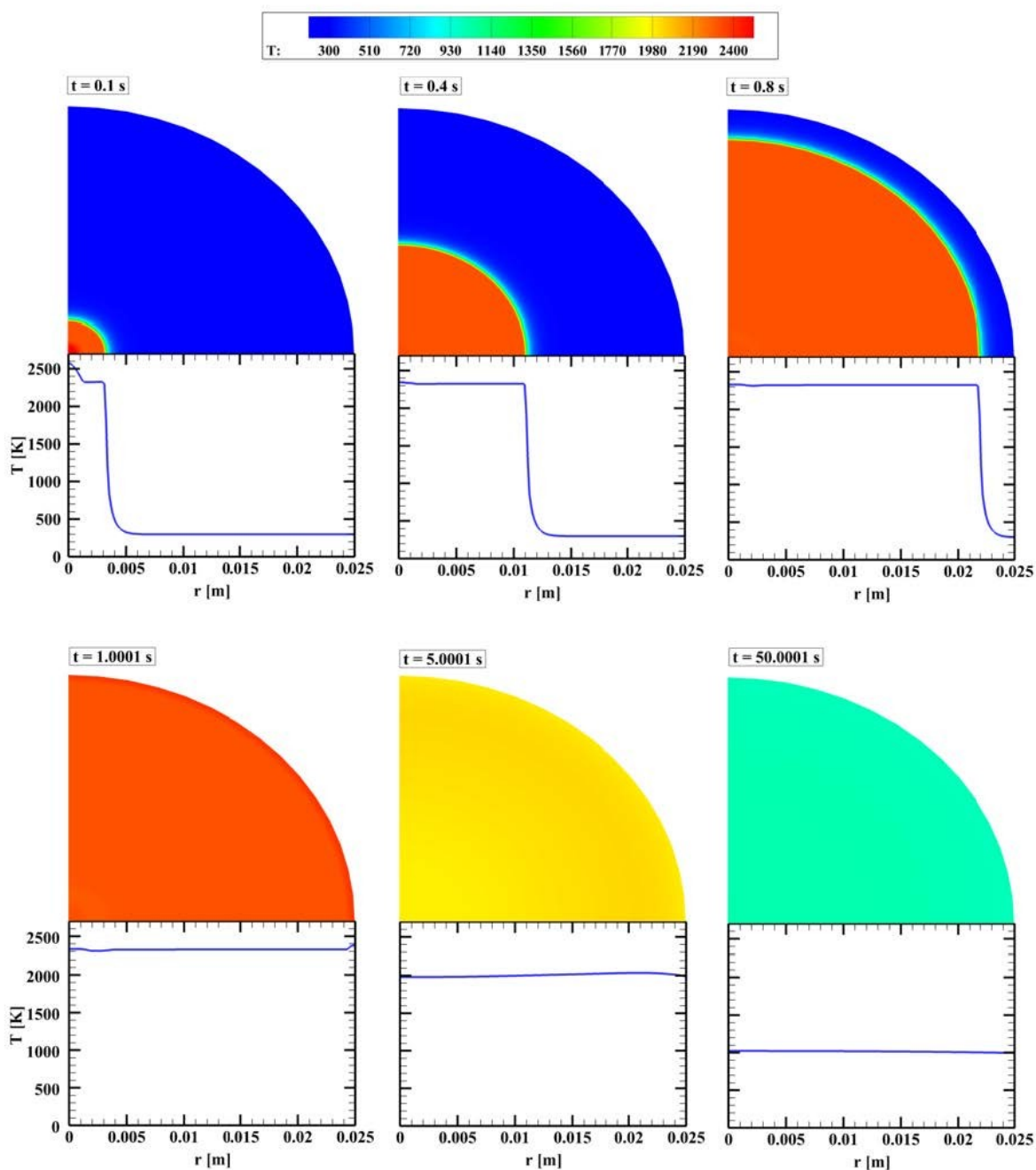


**Figure 10.** Temperature contours and profile as the reaction propagates.

Also, a variation in activation energy affects the wave velocity more drastically than the pre-exponential factor. Observe in Figure 13 that a significant variation of the pre-exponential factor is required to have the same effect in the velocity magnitude as the activation energy, which is explained by the exponential dependence of the reaction rate in the activation energy, as shown in Eq. (18). This analysis will be more clarified next.

By increasing the activation energy by 5% from the initially adopted value of 158 kJ/mol, the wave velocity slows down  $\sim 22\%$ , which is a significant variation. Moreover, an increase of 10% of the activation energy does not allow the reaction wave to be properly evolved, and the self-sustained reaction does not start. These results are presented in Figure 14. As so, the maximum activation energy to evolve the reaction wave observed in the present model is

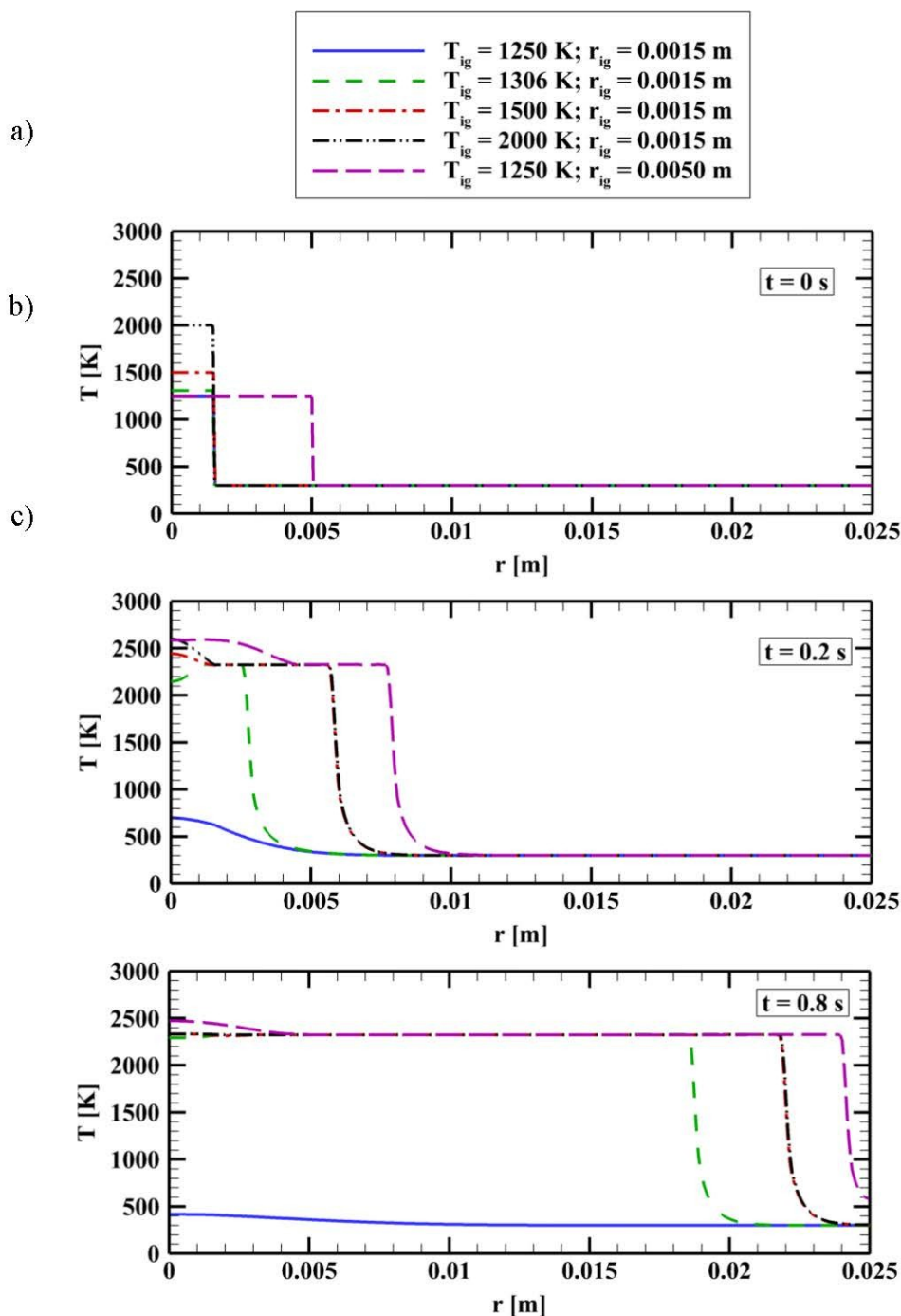


Figure 11. Attempts for the reaction ignition with different initial temperature profiles.

168 kJ/mol, assuming the pre-exponential factor of  $2.2 \times 10^6 \text{ s}^{-1}$ .

The increase of the pre-exponential factor in the same percentage of 5% does not have the same relevant effect as the activation energy, affecting the wave velocity in only  $\sim 3\%$ , as shown in Figure 15. Moreover, these simulated var-

iations on the kinetics parameters have not shown significant effects on the temperature levels reached as the wave propagates through the domain.



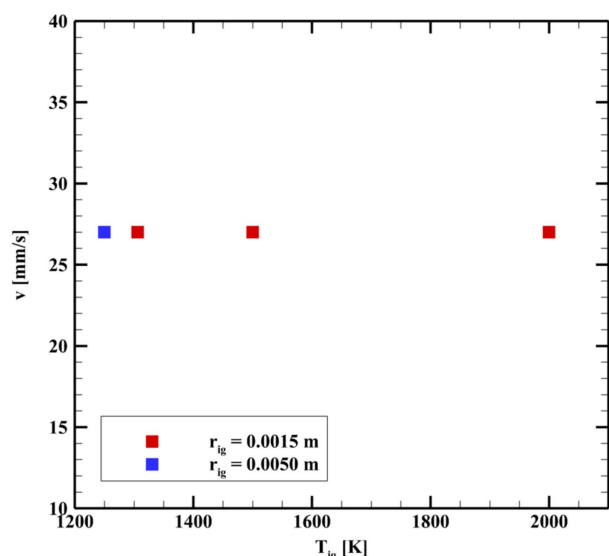


**Figure 12.** Velocity propagation of the reaction wave reached after the wave formation at different ignition temperatures assumed at the ignition zone.

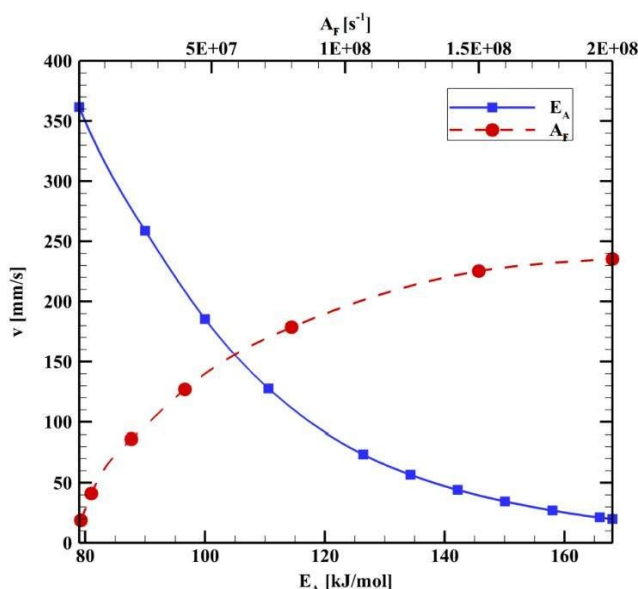


**Figure 13.** Effect of the kinetics parameters on the velocity of the reaction-propagation.

#### 4.4 Validation of the Temperature-Levels

The peak temperatures were compared to the experimental results from Durães *et al.* [31], as observed in Table 3, where they present a difference of 2.9%. It is important to notice that both peak temperatures are close to the fusion temperature of alumina (2327 K). As cited by Kubota [5], the

**Table 3.** Validation of the peak temperature level.

Mean peak temperature observed in the present study	Mean peak temperature measured by Durães <i>et al.</i> [31]	Difference
2325.14 K	2394.65 K	2.9 %

thermite reaction between hematite and aluminum generally results in solid particles of alumina in a liquid iron bath, which does not account for the alumina fusion. As so, we can conclude that the alumina fusion works as a barrier that prevents higher temperatures in the system.

## 5 Conclusions

This work has investigated the front-propagation of the thermite reaction in  $\text{Fe}_2\text{O}_3$ -2Al systems using a finite-difference numerical approach to simulate the reaction and heat transfer in a disk-shaped geometry based on previous literature studies. The kinetics parameters were calibrated to match the reaction-wave velocity propagation measured experimentally in literature, whenever there was data. Phase changes and temperature-dependence of thermodynamic properties were modeled. Validations have been made for the temperature levels at stoichiometric mixtures.

The characteristics of a reaction-front propagation were recognized in the simulations, where two zones were noted: the pre-heating zone, where the heat diffuses through the reaction front and heats the mixture ahead, heating it from ambient temperature to the ignition temperature, which continues the self-sustained reaction; and the reaction zone, which is restricted to a thin layer characterized by rapid consumption of reagents and high-temperature gradients. These observations are in agreement with the literature review.

Finally, a series of simulations were carried out to study the effect of some parameters in the main properties of the reaction front, such as the propagation velocity and peak temperature. These simulations enabled us to reach the following conclusions:

- The Arrhenius parameters, activation energy, and pre-exponential factor are extremely important to correctly predict the reaction-wave velocity since the increase of the activation energy and the decrease of the pre-exponential factor can slow down the reaction speed considerably. However, the activation energy influences the burning velocity much more drastically than the pre-exponential factor;
- The Arrhenius parameters are very singular to each thermite mixture, depending not only on the species involved in the reaction but also on the equivalence ratio. As so, experimental data is required to model a specific thermite reaction with accuracy.

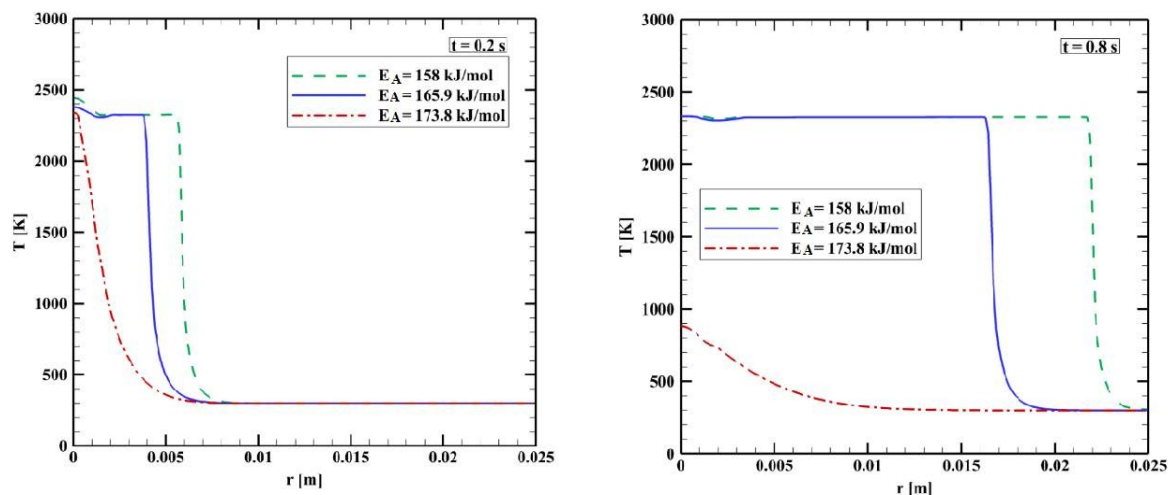


Figure 14. Effect of activation energy in the temperature profile.

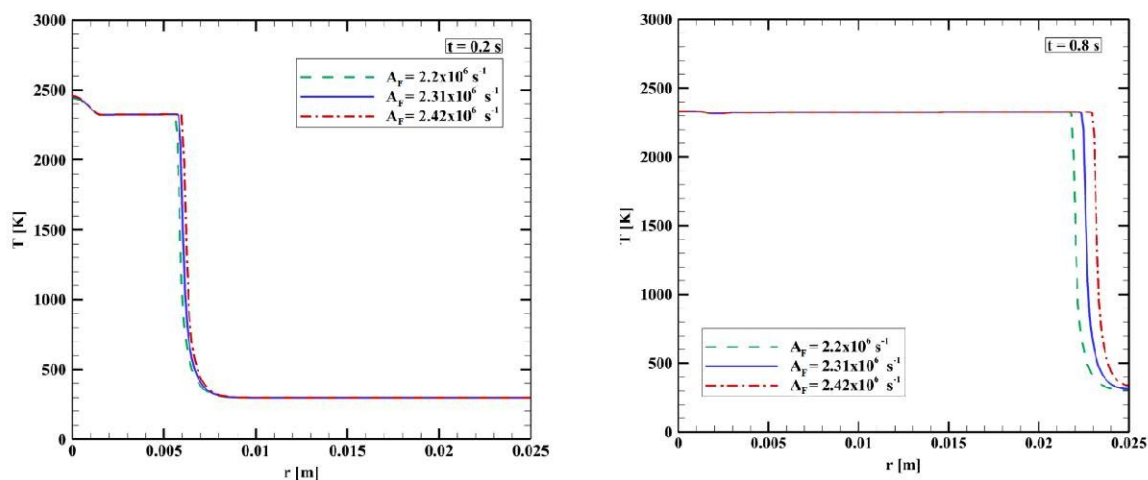


Figure 15. Effect of the pre-exponential factor in the temperature profile.

- The ignition procedure does not affect the burning velocity or the temperature peak reached by the reaction-wave, although it does affect the ignition delay.
- The maximum temperature observed in the model is around the melting temperature of alumina (2327 K), which is in agreement with the experimental results carried out in the literature. This is explained by the fact that the enthalpy of fusion of alumina is very high compared to other thermite species, and the energy generated in the reaction is not enough to fully cover this enthalpy of fusion in a non-adiabatic process, mainly because of the energy losses through conduction.

## Nomenclature

### Latin Characters

$A_F$	Arrhenius pre-exponential factor
$c_p$	Specific heat at constant pressure
$E_A$	Activation energy
$\dot{g}$	Energy generation
$H$	Enthalpy
$H_{\text{reac}}$	Enthalpy of combustion at standard conditions
$i$	$i$ -th radial step
$im$	total amount of radial steps
$k$	Thermal conductivity
$n$	$n$ -th time step
$N$	Order of the reaction
$Q$	Energy released by the reaction

$r$	Radial coordinate
$r_k$	Kinetic rate of reaction
$R$	Ideal gas constant
$S$	Source Term
$T$	Temperature
$T_0$	Initial and outer-ambient temperature.
$t$	Time
$U_{\text{steel/air}}$	Thermal transmittance at the domain bottom-face
$U'_{\text{steel/air}}$	Thermal transmittance at the outer boundary
$U_{\text{PMMA/air}}$	Thermal transmittance at the domain top-face
$v$	Velocity of the front propagation of the reaction
$W$	Mass concentration
$w$	Mass fraction
$Z$	Thickness of the specimen

## Greek Characters

$\Delta r$	Radial step
$\Delta t$	Time step
$\varepsilon$	Emissivity
$\eta$	Extend of reaction
$\sigma$	Boltzmann constant
$\rho$	Density
$\nu$	Volume fraction
$\phi$	Equivalence ratio
$\psi$	Mass stoichiometric coefficient

## Subscripts

$A$	Hematite – $\text{Fe}_2\text{O}_3$
$B$	Aluminum – Al
$C$	Iron – Fe
$D$	Alumina – $\text{Al}_2\text{O}_3$
$E$	Air
$M$	Thermite Mixture
$p$	Products
$r$	Reactants

## Acknowledgments

The authors would like to express their gratitude to CAPES, CNPq, and PETROBRAS, Brazil, for their financial support during the course of this work.

## Data Availability Statement

No Data available.

## References

- [1] J. Mei, R. D. Halldearn, P. Xiao, Mechanisms of the Aluminum-Iron Oxide Thermite Reaction, *Scr. Mater.* **1999**, *41*, 541–548, doi: 10.1016/S1359-6462(99)00148-7.
- [2] S. H. Fischer, M. C. Grubelich, Theoretical Energy Release of Thermites, Intermetallics, and Combustible Metals, *24th International Pyrotechnics Seminar*, July 27–31, **1998**, Monterey, USA, doi: 10.2172/658208.
- [3] G. B. Zanjani, *Synthesis, Characterization, and Application of Nanothermites for Joining*, Master's Thesis, University of Waterloo, Waterloo, Canada, **2013**.
- [4] Y. Meir, E. Jerby, Underwater Microwave Ignition of Hydrophobic Thermite Powder Enabled by the Bubble-Marble Effect, *Appl. Phys. Lett.* **2015**, *107*, 054101, doi: 10.1063/1.4928110.
- [5] N. Kubota, *Propellants and Explosives: Thermochemical Aspects of Combustion*, Wiley-VCH, Weinheim **2007**, 2nd ed.
- [6] W. W. Focke, S. M. Tichapondwa, Y. C. Montgomery, J. M. Grobler, M. L. Kalombo, Review of Gasless Pyrotechnic Time Delays, *Propellants Explos. Pyrotech.* **2018**, *44*, 55–93, doi: 10.1002/prep.201700311.
- [7] H. J. Lunk, Discovery, Properties and Applications of Chromium and its Compounds, *Chem. Tech.* **2015**, *1*, 6, doi: 10.1007/s40828-015-0007-z.
- [8] C. P. Lonsdale, Thermite Rail Welding: History, Process Developments, Current Practices and Outlook for the 21st Century, *AREMA Annual Conf.*, September 12–15, **1999**, Chicago, USA.
- [9] D. Johnson, *Fuel Unit for a Gas Turbine Power Plant*, US Patent 3,516,880, Motors Liquidation Co, Detroit, MI, USA, **1970**.
- [10] P. L. Allen, *Thermite-Resin Binder Solid Fuel Composition*, US Patent 3,309,249, Santa Clara, CA, USA, **1967**.
- [11] D. Belitskus, Aluminothermic Production of Metals and Alloys, *J. Min. Met. Mat. S.* **1972**, *24*, 0–34, doi: 10.1007/BF03355755.
- [12] D. L. Halcomb, J. H. Mohler, *High- and Low- Temperature-Stable Thermite Composition for Producing High-Pressure, High-Velocity Gases*, US Patent 4,963,203, Washington, D. C., USA, **1990**.
- [13] O. Odawara, Metal-Ceramic Composite Pipes Produced by a Centrifugal-Thermite Process, in: *Combustion and Plasma Synthesis of High Temperature Materials* (Eds.: Z. A. Munir, J. B. Holt), Wiley-VCH, New York **1990**.
- [14] D. L. Halcomb, J. H. Mohler, *Low Profile Thermite Igniter*, US Patent 4,996,922, Washington, D. C., USA, **1991**.
- [15] N. C. Hagen, *Method and Device for Thermite Welding at Large Water Depths*, US Patent 6,131,801, Ravnedsveien, Kristiansand, Norway, **2000**.
- [16] F. Alvarez, A. Delgado, J. Frias, M. Rubio, C. White, A. Swamy, E. Shafirovich, Microgravity Combustion of Thermite Mixtures for Welding in Space and for Productions of Structural Materials from Lunar Regolith, *50th AIAA Aerospace Sciences Meeting Including the New Horizons Forum and Aerospace Exposition*, January 09–12, **2012**, Nashville, USA, doi: 10.2514/6.2012-1119.
- [17] M. Skjold, *Method of Well Operation*, WO Patent 2013/135583 A2, Trondheim, Trondelag, Norway, **2013**.
- [18] E. Faierson, K. Logan, B. Stewart, M. Hunt, Demonstration of Concept for Fabrication of Lunar Physical Assets Utilizing Lunar Regolith Simulant and a Geothermite Reaction, *Acta Astronaut.* **2010**, *67*, 38–45, doi: 10.1016/j.actaastro.2009.12.006.
- [19] E. S. Magalhães, M. J. S. de Lemos, A Thermal Study of a New Oil Well Plugging & Abandonment Operation, *Int. J. Therm. Sci.* **2020**, *155*, 106421, doi: 10.1016/j.ijthermalsci.2020.106421.
- [20] G. S. Andrade, M. J. S. de Lemos, D. Colombo, A New Analytical Method for Transient Heat Conduction in Composite Hollow

- Cylinders Applied to Plug and Abandonment of Oil Wells, *Int. J. Therm. Sci. (in press)* **2021**.
- [21] V. Baijot, *Modélisation et Simulation Multi-Niveaux de la Combustion d'une Thermité Composée de Nanoparticules Al/CuO: des Phénomènes Microscopiques à la Simulation du Système en Combustion*, PhD Thesis, Université Toulouse 3 Paul Sabatier, Toulouse, France, **2017**.
- [22] L. Catoire, Detailed Chemical Kinetic Models for Nanothermites Combustion, *Propellants Explos. Pyrotech.* **2018**, *44*, 41–46, doi: 10.1002/prep.201800115.
- [23] S. Knapp, V. Weiser, S. Kelzenberg, N. Eisenreich, Modeling Ignition and Thermal Wave Progression in Binary Granular Pyrotechnic Compositions, *Propellants Explos. Pyrotech.* **2014**, *39*, 423–433, doi: 10.1002/prep.201400023.
- [24] S. Gordon, B. J. McBride, *Computer Program for Calculation of Complex Chemical Equilibrium Compositions, Rocket Performance, Incident and Reflected Shocks, and Chapman-Jouguet Detonations*, Report SP-273, National Aeronautics and Space Administration, Lewis Research Center, Cleveland, OH, USA, **1976**.
- [25] S. Gordon, B. J. McBride, *Computer Program for Calculation of Complex Chemical Equilibrium Composition and Applications*, Report RP-1311, National Aeronautics and Space Administration, Lewis Research Center, Cleveland, OH, USA, **1994**.
- [26] Z. Y. Zhu, B. Ma, C. M. Tang, X. L. Cheng, Molecular Dynamic Simulation of Thermite Reaction of Al Nanosphere/Fe<sub>2</sub>O<sub>3</sub> Nanotube, *Phys. Lett. A* **2016**, *380*, 194–199, doi: 10.1016/j.physleta.2015.09.041.
- [27] V. Baijot, L. Glavier, J. M. Ducéré, M. D. Rouhani, C. Rossi, A. Estève, Modeling the Pressure Generation in Aluminum Based Thermites, *Propellants Explos. Pyrotech.* **2015**, *40*, 402–412, doi: 10.1002/prep.201400297.
- [28] K. S. Martirosyan, M. Zyskin, C. M. Jenkins, Y. Y. Horie, Modeling and Simulation of Pressure Waves Generated by Nano-Thermite Reactions, *J. Appl. Phys.* **2012**, *112*, 094319, doi: 10.1063/1.4764319.
- [29] S. Brotman, M. D. Rouhani, C. Rossi, A. Esteve, A Condensed Phase Model of the Initial Al/CuO Reaction Stage to Interpret Experimental Findings, *J. Appl. Phys.* **2019**, *125*, 035102, doi: 10.1063/1.5063285.
- [30] L. Durães, P. Brito, J. Campos, A. Portugal, Modelling and Simulation of Fe<sub>2</sub>O<sub>3</sub>/Aluminum Thermite Combustion: Experimental Validation, *Comput. Aided Chem. Eng.* **2006**, *21*, 365–370, doi: 10.1016/S1570-7946(06)80073-8.
- [31] L. Durães, J. Campos, A. Portugal, Radial Combustion Propagation in Iron(III) Oxide/Aluminum Thermite Mixtures, *Propellants Explos. Pyrotech.* **2006**, *31*, 42–49, doi: 10.1002/prep.200600006.
- [32] P. Brito, L. Durães, J. Campos, A. Portugal, Modelling and Simulation of Fe<sub>2</sub>O<sub>3</sub>/Al Thermite Combustion, *9th International Chemical Engineering Conference*, September 21–23, **2005**, Coimbra, Portugal.
- [33] S. V. Patankar, *Numerical Heat Transfer and Fluid Flow*, CRC Press, Boca Raton **1980**.
- [34] M. Chase Jr., C. Davies, J. Downey Jr., D. Frurip, R. McDonald, A. Syverud, *JANAF Thermochemical Tables*, 3rd ed., J. Phys. Chem. Ref. Data, **1985**, vol. 14, suppl. 1.
- [35] C. Bonacina, G. Comini, A. Fasano, M. Primicerio, Numerical Solution of Phase-Change Problems, *Int. J. Heat Mass Transfer* **1973**, *16*, 1825–1832, doi: 10.1016/0017-9310(73)90202-0.
- [36] Y. Qu, Y. Yang, Z. Zou, C. Zeilstra, K. Meijer, R. Boom, Thermal Decomposition Behavior of Fine Iron Ore Particles, *ISIJ Int.* **2014**, *54*, 2196–2205, doi: 10.2355/isijinternational.54.2196.
- [37] M. J. S. de Lemos, Numerical Simulation of Turbulent Combustion in Porous Materials, *Int. Commun. Heat Mass Transfer* **2009**, *36*, 996–1001, doi: 10.1016/j.icheatmasstransfer.2009.07.006.
- [38] L. A. Tofaneli, M. J. S. de Lemos, Double-Diffusive Turbulent Natural Convection in a Porous Square Cavity with Opposing Temperature and Concentration Gradients, *Int. Commun. Heat Mass Transfer* **2009**, *36*, 991–995, doi: 10.1016/j.icheatmasstransfer.2009.06.018.
- [39] N. Sbirrazzuoli, L. Vincent, S. Vyazovkin, Comparison of Several Computational Procedures for Evaluating the Kinetics of Thermally Stimulated Condensed Phase Reactions, *Chemom. Intell. Lab. Syst.* **2000**, *54*, 53–60, doi: 10.1016/S0169-7439(00)00103-9.
- [40] S. K. Sahoo, S. M. Danali, P. R. Arya, Ignition Behavior of Al/Fe<sub>2</sub>O<sub>3</sub> Metastable Intermolecular Composites, *Int. J. Eng. Res. Sci.* **2017**, *3*, 61–71, doi: 10.25125/engineering-journal-IJOER-NOV-2017-12.
- [41] C. Bodsworth, A. S. Appleton, *Problems in Applied Thermodynamics*, Longmans, London **1965**, p. 37–39.
- [42] C. A. J. Fletcher, *Computational Techniques for Fluid Dynamics 1: Fundamental and General Techniques*, Berlin **1991**, Springer, 2nd ed.
- [43] A. Nieckele, *Solução de Sistema Algébrico*, Pontifical Catholic University of Rio de Janeiro, **2015**, available in: [http://mecflu2.usuarios.rdc.puc-rio.br/Din\\_Flu\\_Comp\\_Mec2335/V-dfc-SistemaAlgebrico.pdf](http://mecflu2.usuarios.rdc.puc-rio.br/Din_Flu_Comp_Mec2335/V-dfc-SistemaAlgebrico.pdf).
- [44] Bloodshed, *Dev C++ 5.11 Released*, Orwell, GNU General Public License, **2015**, available in: <http://orwelldevcpp.blogspot.com/>.
- [45] K. Kim, Computational Modeling of Combustion Wave in Nanoscale Thermite Reaction, *Int. J. Energy Power Eng.* **2014**, *8*, 679–682, doi: 10.5281/zenodo.1093924.
- [46] Y. Zhang, G. C. Stangle, Ignition Criteria for Self-Propagating Combustion Synthesis, *J. Mater. Res.* **1993**, *8*, 1703–1711, doi: 10.1557/JMR.1993.1703.
- [47] Y. Meir, E. Jerby, Thermite Powder Ignition by Localized Microwaves, *Combust. Flame* **2012**, *159*, 2474–2479, doi: 10.1016/j.combustflame.2012.02.015.
- [48] H. Sui, *Investigation on Reaction Mechanisms of Nano-Energetic Materials and Application in Joining*, PhD Thesis, University of Waterloo, Waterloo, Canada, **2019**, p. 6–7.
- [49] J. Cheng, H. H. Hng, Y. W. Lee, S. W. Du, N. N. Thadhani, Kinetic Study of Thermal- and Impact- Initiated Reactions in Al-Fe<sub>2</sub>O<sub>3</sub> Nanothermite, *Combust. Flame* **2010**, *157*, 2241–2249, doi: 10.1016/j.combustflame.2010.07.012.
- [50] B. Sarangi, A. Sarangi, H. S. Ray, Kinetics of Aluminothermic Reduction of MnO<sub>2</sub> and Fe<sub>2</sub>O<sub>3</sub>: A Thermoanalytical Investigation, *ISIJ Int.* **1996**, *36*, 1135–1141, doi: 10.2355/isijinternational.36.1135.

Manuscript received: October 27, 2020

Revised manuscript received: December 16, 2020

Version of record online: February 10, 2021